A super-refractory inclusion containing non-stoichiometric spinel from the CO3.0 chondrite Yamato 81020

Hisayoshi Yurimoto[1*], Alan E. Rubin[2], Shoichi Itoh[3] and John T. Wasson[2]

[1]Isotope Imaging Laboratory (IIL), Natural History Sciences, Hokkaido University, Sapporo 001-0021, Japan

[2]Department of Earth, Planetary, and Space Sciences, University of California, Los Angeles, CA 90095-1567, USA

[3]Department of Earth and Planetary Sciences, Kyoto University, Kyoto 606-8502, Japan

* Corresponding author. E-mail: yuri@ep.sci.hokudai.ac.jp

Submitted to MAPS (January 9, 2021)

Abstract

We studied a unique super-refractory inclusion with a core-mantle structure from CO3.0 Yamato 81020 by secondary ion mass spectrometry (SIMS), electron microprobe and scanning electron microscope techniques. The core consists largely of hibonite and nonstoichiometric Al-rich spinel indicating formation as a liquid at an exceptionally high temperature (>1900 °C). The mantle consists almost entirely of melilite with gehlenitic compositions (ranging from $Åk_2$ to $Åk_{25}$). The oxygen- and magnesium-isotopic compositions of the core and mantle are very different; typically, $\Delta^{17}O$ ($\equiv \delta^{17}O - 0.52\ \delta^{18}O$) ~−26 ‰ and f_{Mg} (mass fractionation of Mg isotopes) ~10 ‰/amu in the core and $\Delta^{17}O$ ~−7 ‰ and f_{Mg} ~1 ‰/amu in most of the mantle. The chemical and O, Mg-isotopic data indicate that the core and mantle formed in separate events, and that the melilite now in the core was formed during the mantle-melting event, probably filling preexisting voids and surficial cavities. Analyses of core and mantle phases plot along a single ^{26}Al–^{26}Mg isochron with initial $(^{26}Al/^{27}Al)_0$ corresponding to 4.8 ±1.0 (±2σ) × 10^{-5}, suggesting similar formation age to normal CAIs in chondrites.

Keywords: O-16; Al-26; refractory inclusion; chondrite; solar nebula

Introduction

Refractory (Ca-Al-rich) inclusions (CAIs) in chondritic meteorites are widely believed to be the first solid objects formed in the solar nebula (Connelly et al., 2012). The most distinctive characteristics of refractory inclusions are their refractory mineral phases (e.g., Grossman and Larimer, 1974), ^{16}O-rich isotopic signatures (Clayton, 1993; Yurimoto et al., 2008) and, in many cases, isotopic records of the decay products of short-lived radio-nuclides such as ^{26}Al (MacPherson et al., 1995). Recent in-situ isotope microanalysis has allowed identification of the detailed isotopic variations of minerals in refractory inclusions. Variations of ^{16}O-rich isotopic signatures have been interpreted to be records of: (i) condensation from the solar nebular gas with variable O-isotopic compositions for condensate CAIs (Katayama et al., 2012; Kawasaki et al., 2017; Kawasaki et al., 2012; Park et al., 2012); (ii) multiple partial melting and associated O-isotope exchange between the melt and solar nebular gas for igneous CAIs (Aléon, 2016; Aléon et al., 2007; Ito et al., 2004; Kawasaki et al., 2015; Kawasaki et al., 2018; Krot et al., 2008; Krot et al., 2014; Wakaki et al., 2013; Yoshitake et al., 2005; Yurimoto et al., 1998); (iii) O-isotope exchange by solid-state diffusion at high temperatures in solar nebular gas after solidification (Clayton et al., 1977; Simon et al., 2011; Simon et al., 2016); and (iv) chemical exchange of O-isotopes under aqueous conditions on chondrite parent bodies (Kawasaki et al., 2015; Kawasaki et al., 2018; Krot et al., 2008; Krot et al., 2019; Krot

et al., 2014; Park et al., 2012; Yoshitake et al., 2005). The O-isotope disequilibrium in coarse-grained CAIs may also have resulted from a combination of such processes that could have varied among individual CAIs (Kawasaki et al., 2018). Small and fine-grained CAIs also have variable ^{16}O-rich signatures that originated by processes similar to those described above (Aléon et al., 2005; Bodénan et al., 2014; Itoh et al., 2004; Krot et al., 2002; McKeegan et al., 1998; Sakai and Yurimoto, 1999; Ushikubo et al., 2017; Wada et al., 2020; Wasson et al., 2001); the primary phases of these inclusions also contain the decay products of short-lived nuclides (Kawasaki et al., 2020).

Spinel is a common mineral in refractory inclusions. The spinel composition is stoichiometric $MgAl_2O_4$ independent of the type of refractory inclusion. Nonstoichiometric Al-rich spinel, however, is reported from several super-refractory inclusions (El Goresy et al., 1984; Simon et al., 1994). The highest reported amount of excess Al_2O_3 in spinel solid solution is ~10 mol%. On the other hand, a much wider range of spinel solid solution, with up to ~80 mol% excess Al_2O_3, has been synthesized by laboratory experiments (e.g., Hallstedt, 1992). The solubility of Al_2O_3 in the spinel solid solution increases with increasing temperature for the system $MgAl_2O_4$-Al_2O_3 (Shirasuka and Yamaguchi, 1974; Viechnicki et al., 1974; Viertel and Seifert, 1980). The differences of the solid solution range of spinel between nature and laboratory is an unsolved issue and may provide a new approach to understanding the origin of refractory inclusions.

Here we describe a unique refractory inclusion in the pristine CO3.0 chondrite Yamato 81020. The inclusion has high modal abundances of Al_2O_3-rich components and contains nonstoichiometric Al-rich spinel as a major mineral. The large nonstoichiometric feature has not been reported previously in natural spinel. We also measured the O-isotopic compositions and Al-Mg isotopic systematics of the inclusion to elucidate its origin.

Experimental

We studied a thin section of Yamato 81020-56-4 from the National Institute for Polar Research in Tokyo. A back scattered electron (BSE) image of the CAI was prepared from the carbon coated section using the LEO 1430 scanning electron microscope (SEM) at the University of California, Los Angeles (UCLA) and the JEOL 5310LV SEM at the Tokyo Institute of Technology (TiTech). Elemental compositions were determined using wavelength dispersive spectrometry (WDS) on the UCLA Cameca Camebax electron microprobe (EPMA) and by energy dispersive spectrometry (EDS) on the SEM with the TiTech Oxford LINK ISIS. There was good agreement between the two sets of compositional data. Because we found nonstoichiometric spinels, we routinely checked the quantitative precision by including stoichiometric spinel in the same analytical runs. The mineral composition data in Table 1 were obtained using the WDS system; those in Table 2 and Fig. 1 were collected using the EDS system.

The oxygen- and magnesium-isotope microanalyses were performed by secondary ion mass spectrometry (SIMS) with the TiTech Cameca ims-1270 instrument (this instrument is now installed at Hokkaido University). The analytical procedures were described earlier (Yurimoto et al., 1998). For the measurement of O isotopes, the primary ion beam consisted of mass-filtered positive 20 keV Cs^+ ions; the typical spot size was 5 μm. The primary beam current was ~3 pA, adjusted to obtain a count rate of ~4×10^5 cps for negative ^{16}O ions. A normal incidence electron gun was utilized for charge compensation. Negative secondary ions corresponding to the ^{16}O tail, ^{16}O, ^{17}O, ^{16}OH and ^{18}O were analyzed by an electron multiplier (EM) at a mass resolution of ~6000. Obtained count rates were corrected for the EM dead time. A spinel standard, SPU, was used and the data normalized to the SMOW standard (Koike et al., 1993; Yurimoto et al., 1994). Typical errors ($2\sigma_m$) for $\delta^{17}O$, $\delta^{18}O$ and $\Delta^{17}O$ were 5 ‰, 3 ‰ and 6 ‰, respectively.

For Mg isotopes the primary ion beam consisted of 23 keV $^{16}O^-$ ions. The beam diameter was 5 μm. Primary beam currents ranged from 30 to 60 pA and were adjusted for each run to obtain a $^{27}Al^+$ or $^{24}Mg^+$ count rate of not more than ~4×10^5 cps. Positive secondary ions corresponding to ^{24}Mg, ^{25}Mg, ^{26}Mg and ^{27}Al were analyzed by the EM at a mass resolution of ~4500. Obtained count rates were corrected for the EM dead time. The following terrestrial values are used for the Mg-isotope corrections: $^{25}Mg/^{24}Mg=0.12663$, $^{26}Mg/^{24}Mg=0.13932$ (Catanzaro et al., 1966). Variations of terrestrial mass

fractionation of Mg-isotopes among spinel, hibonite and melilite were evaluated using the SPU, Madagascar hibonite and synthetic åkermanite standards, respectively. The degree of instrumental mass fractionation was the same for melilite and spinel within analytical errors, but was 4 ‰/amu larger for hibonite than those for melilite under the analytical conditions.

Petrography and mineral chemistry of Tama

A unique refractory inclusion of 200×180 μm^2 is located in the section NIPR 56-4 of the Yamato 81020 CO3.0 chondrite (Fig. 1). There is a tradition to name unique refractory inclusions (e.g., Armstrong et al., 1982). This refractory inclusion has an ovoid-shaped core and is, in our opinion, a gem; we therefore gave it the Japanese name Tama, a word that includes both of these meanings.

Tama has a core-mantle structure and a minimal porosity (Fig. 1). In the polarized transmitted light image with a sensitive color plate (Fig. 1b), the hibonite appears blue, the spinel brown, and melilite mostly blue and brown. The ovoid core (170×80 μm^2) is composed of hibonite (~50 vol%), anhedral Al-rich spinel (~42 vol%), melilite (~6 vol%), perovskite (<1 vol%), and an alumina-rich patch (~2 vol%).

The mantle is composed mainly of coarse-grained (long dimension up to 100 μm) clear melilite crystals (Fig. 1b). The melilite mantle largely surrounds the core (it is missing on the lower left), but it is much thicker on the upper left side of the image.

We divided the thick part of the mantle into seven individual single crystal grains based on the extinction angle in polarized transmitted light; these grains are labeled A-G, with A being the largest grain (100×60 μm^2) (Fig. 1c). The mantle melilite contains some perovskite crystals although the abundance is smaller than in the core. A thin layer of melilite at the outer edge of the mantle and at the boundary between the core and the enveloping mantle has been partly converted to submicrometer-size alteration products, probably nepheline and FeO-rich pyroxenes.

Several small patches on the left edge of the mantle contain hibonite, Al-rich spinel, and the alumina-rich patch. They are inferred to be derived from one or more fragments dislodged from the core. If these are all parts of a single entity (most of which was not in the plane of the section), its length was at least 100 μm. We designate these areas "core satellites". Grossite was observed only at one point on the interface between the large core satellite and the mantle.

Representative chemical compositions of each mineral are given in Table 1 and chemical zoning is illustrated in Fig. 1c. The hibonite has the composition $Ca(Al, Mg)_{12-x}Ti_xO_{19}$; $0<x<1$, $0.94<Al/(Al+Mg)<0.99$. The spinel is highly non-stoichiometric with excesses of Al_2O_3 (Fig. 2). Non-stoichiometric spinel has been observed in CAIs, but the excess Al_2O_3 ranges only up to 10 mol% (El Goresy et al., 1984). The excess Al_2O_3 of spinel from Tama ranges from 23 mol% to 77 mol%. Such solid solution ranges of spinel crystals have been synthesized by

laboratory experiments (Shirasuka and Yamaguchi, 1974; Viechnicki et al., 1974). If we write the formula: $Mg_{1-3x}Al_{2+2x}Va_xO_4$, $0.08<x<0.26$; then the ratio $Al_2O_3/(MgO+Al_2O_3)$ = 59–86 mol% or 79–94 wt%. The excess Al_2O_3 is large at the edge of the spinel grains and small in the center (Fig. 1c). Therefore, it appears that the excess Al_2O_3 increased during crystal growth. The largest excess Al_2O_3 of spinel is in contact with the alumina-rich patch.

The alumina-rich patch shows variable small amounts of MgO components of less than 4 wt% (Table 1). It proved very difficult to characterize phases in the alumina-rich patch; it shows very little contrast relative to the adjacent spinel in secondary electron and back-scattered electron images. Analysis of about 30 points by EPMA yielded two points with compositions close to pure Al_2O_3 (a representative analysis is in Table 1); all other points have high (2-4 wt%) MgO contents, possibly indicating beam overlap with spinel (Fig. 2). Because of this, even the reported MgO contents of the two purest alumina-phase grains must be considered upper limits, but within the limit of solubility of MgO in corundum, ~0.4 wt% (Viechnicki et al., 1974). We infer that the grain size of the almost-pure Al_2O_3 is small (<3 μm). We suggest that the numerous analyses showing MgO contents in the 2-4% range all consist of two-phase mixtures of corundum and spinel (Fig. 2). If this is correct, then the alumina-rich patch is a fine-grained aggregate consisting of corundum and spinel, with a bulk composition that can be written as $Al_2O_3 \cdot xMgO$, $x<0.11$.

Melilite in the core is almost pure gehlenite ($Ca_2Al_2SiO_7$); it contains only 1–2 mol% åkermanite ($Ca_2MgSi_2O_7$). The melilite is in contact both with hibonite and spinel. The mantle melilite is zoned from $Åk_2$ to $Åk_{25}$ (Fig. 1c); the zoning crosses grain boundaries. The gehlenitic compositions occur at the grain boundaries suggesting reverse zoning (MacPherson and Grossman, 1984).

O and Mg isotopes of Tama

We measured O- and Mg-isotopic compositions of hibonite, spinel and melilite in Tama (Tables 2 and 3); we were unable to measure the isotopic compositions of perovskite, grossite and corundum because of their small grain sizes. All O-isotopic compositions of Tama scatter along the carbonaceous-chondrite anhydrous minerals (CCAM) line defined by Clayton (1993) (Fig. 3).

The O-isotopic compositions of core hibonite and spinel are homogeneous and enriched in ^{16}O ($\Delta^{17}O \equiv \delta^{17}O_{SMOW} - 0.52\ \delta^{18}O_{SMOW} = -30$ to -26 ‰). In contrast, melilite in the core region shows a range of ^{16}O-rich compositions ($\Delta^{17}O = -26$ ‰ to -16 ‰). The ^{16}O-rich end member of core melilite seems to be slightly ^{16}O-poor relative to the values of hibonite and spinel. Variations in the O-isotopic composition of mantle melilite ($\Delta^{17}O$ values range from -20 ‰ to -2 ‰) do not correlate with the position of the melilite grains in Tama such as distance from the outer rim, from the core-mantle boundary, or from hibonite or spinel. However, $\Delta^{17}O$ correlates positively with the Åk content of the melilite below Åk = 5 mol%; at high Åk (>6 mol%) there is no

resolvable change in the $\Delta^{17}O$ values, around a mean value of ~−7‰ (Fig. 4).

Mass fractionation of Mg isotopes (f_{Mg}) is different between core spinel or hibonite and (core and mantle) melilite (Table 3). The f_{Mg} of hibonite and spinel is greater than 10 ‰/amu, but f_{Mg} of melilite is less than 5 ‰/amu (the mean is 1.2 ‰/amu). The excess ^{26}Mg was observed from melilite, hibonite and Al-rich spinel (Fig. 5). The plots form a linear array with $^{27}Al/^{24}Mg$. The initial $(^{26}Al/^{27}Al)_0$ ratio and initial $(\delta^{26}Mg)_0$ are 4.8 ±1.0 (2σ) $\times10^{-5}$ and 1.4 ±1.7 (2σ) ‰, respectively. The initial ratios are consistent with the canonical values of the CAIs (Larsen et al., 2011).

Crystallization sequence of Tama

An Al-excess in spinel solid solution of the magnitude observed in Tama has not been reported previously in refractory inclusions, although it is known from laboratory experiments (Mendybaev et al., 2006; Shirasuka and Yamaguchi, 1974; Viechnicki et al., 1974). The spinel with the greatest Al-excess coexists with corundum in the alumina-rich patch (Fig. 1c). The spinel grew as a solid solution crystal from Al-excess-poor core to Al-excess-rich rim. This relationship is unexpected from the system $MgAl_2O_4$-Al_2O_3 (Hallstedt, 1992; Shirasuka and Yamaguchi, 1974; Viechnicki et al., 1974) if corundum preexisted and spinel formed as the second phase with decreasing temperature; this is because the composition of spinel normally changes from Al-excess-rich to Al-excess-poor during

crystal growth. However, this relationship is realized if spinel crystalizes as a liquidus phase in the system $MgAl_2O_4$-Al_2O_3 and corundum crystallizes as a second liquidus phase by fractional crystallization. The round shape of Tama is likely a result of surface tension, thus supporting a liquid origin for the minerals.

The bulk compositions of Tama calculated from the modes and the mean compositions of the minerals are Al_2O_3: 55 mol% (71 wt%), CaO: 22 (16), MgO: 13 (6), SiO_2: 10 (7) for the whole CAI and Al_2O_3: 72 mol% (85 wt%), CaO: 10 (6), MgO: 17 (8), SiO_2: 1 (1) for the core. It is Al_2O_3: 74 mol% (87 wt%), CaO: 8 (5), MgO: 18 (8) for the core if melilite is excluded. In a liquid having the bulk composition of the whole CAI, hibonite should be the first liquidus mineral (Beckett and Stolper, 1994). Then spinel, grossite and melilite would crystallize sequentially. Non-stoichiometric spinel would not be predicted by phase equilibria, which is inconsistent with the observed composition. Moreover, grossite is rare in Tama, and was observed only at one point on the interface between the large core satellite and the mantle. Furthermore, differences of O-isotopic composition and f_{Mg} between spinel or hibonite and melilite are also implausible if they crystallized from the same liquid.

Crystallization from a liquid having the core composition cannot be evaluated using the phase diagram of Beckett and Stolper (1994) because the core SiO_2 composition is too low; the core composition plots in their hibonite-unstable field. Instead of their diagram, the system Al_2O_3-MgO-CaO (De Aza et al., 2000) would be

applicable. The core composition (open circle of Fig. 6) plots in the spinel liquidus field close to the intersection of eutectic or cotectic lines of spinel and corundum or hibonite. Crystallization from a liquid having the core composition starts with spinel, then switches to coprecipitation of spinel and hibonite. Small amounts of corundum may be precipitated before hibonite crystallization if we allow for uncertainties in the estimated bulk composition. The true core composition may be more depleted in CaO because the O-isotopic composition and f_{Mg} of the melilite are different from those of spinel and hibonite. If so, then the core composition would shift from the open circle to the solid circle in Fig. 6. The solid circle corresponds to the composition that is free from the melilite contribution. Then, the crystallization sequence is spinel(ss), corundum, hibonite and grossite, consistent with the petrography of the core. Moreover, the degree of excesses Al_2O_3 of spinel(ss) is in agreement with the experimental results of De Aza et al. (2000).

According to Fig. 6, the crystallization temperature of the first spinel is about 1900 °C; it follows that the Tama core experienced temperatures at least this high. This liquidus temperature is similar to that of CAI B6 and ~100 °C lower than that of CAI BB-2 according to recent experimental results (De Aza et al., 2000) instead of calculated results (Simon et al., 1994). This temperature is at least 300 °C higher than that at which this liquid would be stable relative to evaporation in a nebula of solar composition, even at an implausibly high pH_2 of 10^{-2} atm (Yoneda and

Grossman, 1995). We therefore infer that the core was melted during a rapid heating/cooling event.

The core composition is Al_2O_3-rich and SiO_2-poor compared with typical CAIs. Moreover, the MgO concentration is higher than that of CaO. Calculations of the condensation/evaporation sequence for solids (Yoneda and Grossman, 1995) show that, in a canonical nebula at a pH_2 of 10^{-5} atm, corundum condenses first followed by hibonite and perovskite. After the temperature falls another 50 °C to ~1200 °C, gehlenitic melilite ($Ca_2Al_2SiO_7$) condenses, followed by spinel ($MgAl_2O_4$) at about 1080 °C. At the condensation temperatures of melilite and spinel, spinel should not show such large excess-Al_2O_3 even if it coexisted with corundum (Shirasuka and Yamaguchi, 1974). Thus, this condensation process cannot account for the composition of the spinel(ss) and the f_{Mg} of the minerals in the core.

On the other hand, in nature, corundum-, hibonite-, spinel-bearing CAIs that are melilite-free or very melilite-poor are commonly found in carbonaceous chondrites (El Goresy et al., 1984; Han et al., 2015; MacPherson et al., 1983; MacPherson and Davis, 1994; Makide et al., 2013; Simon et al., 2006; Simon et al., 1994). Some of these CAIs clearly formed by crystallization from a melt derived from precursor phases that probably condensed from nebular gas (El Goresy et al., 1984; MacPherson et al., 1983; Simon et al., 2006; Simon et al., 1994). Some of them clearly show evidence that their primary phases formed by direct condensation from nebular gas (Han et al., 2015; MacPherson and Davis, 1994; MacPherson et al., 1984).

In order to form the precursor CAIs, condensation of spinel should occur prior to that of melilite. This condensation sequence inferred by paragenesis of the CAIs is obviously inconsistent with equilibrium condensation (Yoneda and Grossman, 1995). The mechanism has been unknown although kinetic controls would likely play important roles (Beckett and Stolper, 1994; MacPherson and Davis, 1994; Simon et al., 2006).

The consistency among interpretations based on isotopic evidence, core composition, petrography, the phase diagram and condensation equilibria support the conclusion that the first material in Tama was a liquid having the core composition and that the mantle formed later. The melilite now in the core region was not present when the core formed, but was added later, filling surficial cavities produced during core solidification or selective dissolution of the core during mantle formation. This process is also supported by the isotopic evidence observed in Tama.

From the distinct isotopic compositions between melilite and spinel or hibonite of Tama, the mantle formed after the core. Smooth and round outlines of the mantle suggest that the mantle formed from liquid (Fig. 1). The compact connections with straight grain boundaries between melilite crystals support the liquid origin of the mantle. If this is correct, then precursor solids would have existed around the solidified core before mantle melting because condensation of melt is highly implausible in a canonical nebula (Yoneda and Grossman, 1995). The precursors would be composed mainly

of melilite. Condensation of melilite at a temperature lower than the core-formation temperature is possible in a canonical nebula (Wada et al., 2020; Yoneda and Grossman, 1995). We will discuss the formation of reversely zoned melilite from the melt in the next section.

Possible formation scenarios for Tama

A conceivable scenario of the formation of Tama is as follows: (1) melting of a precursor CAI at temperatures >1900 °C, (2) partial evaporation of the liquid droplet, (3) crystallization of the liquid droplet to form the core, (4) condensation of melilite around the core at a temperature of ~1200 °C, (5) melting of the melilite by reheating to a temperature of ~1600 °C, and (6) mantle melilite crystallization from this liquid to fill cavities in the core.

The core would have crystallized from a melt composed of precursor solids that condensed from the solar nebular gas. The precursor would be a corundum-, hibonite-, spinel-bearing CAI containing very little or no melilite with a bulk composition similar to those of B6 or BB2 CAIs (Fig. 6). The melting occurred at the age of normal CAI formation corresponding to the canonical $(^{26}Al/^{27}Al)_0$ ratio in Tama: 4.8 ±1.0 (2σ) $\times 10^{-5}$. When the precursor melted at temperatures >1900 °C, significant selective evaporation of MgO occurred from the liquid droplet due to the less-refractory nature of this component compared to CaO and Al_2O_3 (Davis et al., 1998; Hashimoto, 1983). This model is supported by the observed

fractionation of the Mg isotopes; f_{Mg} > 10 ‰/amu, i.e., enrichment of heavy isotopic components of Mg by Mg loss. There are at least two plausible origins for the ^{16}O-rich signature (Δ^{17}O ~ −26‰) of the core: (1) The ^{16}O-rich signature could have been inherited from the precursor materials if the evaporation process was carried out under conditions that did not permit exchange with the gas (e.g., very low gas pressures or a very short melt lifetime). Such an ^{16}O-rich signature is common for fine-grained CAIs of CO chondrites and other chondrite groups (Itoh et al., 2004; Yurimoto et al., 2008). (2) The Δ^{17}O of the gas was about −26‰ when the core formed if O-isotope exchange between liquid and gas was relatively rapid. Spinel(ss), corundum, hibonite and grossite crystallized sequentially from the liquid, and then solidified at ~1730 °C (De Aza et al., 2000).

At ~1200 °C, melilite condensed directly on the solidified core to produce the mantle precursor in the cooling solar nebula (Yoneda and Grossman, 1995). A recent study suggests that the oxygen-isotopic compositions of melilite condensed from the solar nebula had variable Δ^{17}O values ranging from −23 ‰ to 0 ‰ (Wada et al., 2020). Tama was then reheated to a temperature of ~1600 °C and the mantle precursor materials were melted. A small amount of the core minerals may have dissolved within the mantle melt during this event. The melilite crystallized from the melt with a growth style exhibiting reverse zoning (Fig. 1). The reverse zoning suggests that the composition of the melt gradually became enriched in Al while melilite was crystallizing. There may be two possible origins for the Al

enrichment of the melt: (1) evaporation of the melt, reducing the amount of Mg and Si (Mendybaev et al., 2006), or (2) assimilation between the melt and the Al-rich core.

CO3.0 chondrites including Yamato 81020 have experienced minimal aqueous alteration; melilite in their fine-grained inclusions has $\Delta^{17}O$ values <–20‰ (Itoh et al., 2004; Wasson et al., 2001). These workers attributed more ^{16}O-poor values observed in fine-grained melilites from higher CO3 petrographic subtypes to parent-body aqueous alteration. It therefore seems clear that the oxygen-isotopic composition of the coarse melilite mantle of Tama was established in the solar nebula, not in the parent asteroid.

During this high-temperature period, melilite started to crystallize with $\Delta^{17}O$ = –7 ‰ (Fig. 4), suggesting that O-isotopic exchange occurred between the melt and the nebular gas (Yurimoto et al., 1998). The O-isotopic composition of the nebular gas became ^{16}O-rich during melilite crystallization and the melt gradually equilibrated its O isotopes with those of the gas (if the reverse zoning was caused by evaporation). The O-isotopic composition of the melt changed towards ^{16}O-rich (if the reverse zoning has an assimilation origin). In either case, the Mg-Al systematics (Fig. 5) suggest that ^{16}O-rich and ^{16}O-poor reservoirs existed contemporaneously within the resolution of the Al-Mg system in the solar nebula during the earliest stages of solar-system history.

Summary

A unique super-refractory inclusion named Tama with a core-mantle structure was found in CO3.0 Yamato 81020. The core consists largely of nonstoichiometric Al-rich spinel and hibonite. The mantle consists almost entirely of melilite with gehlenitic compositions (ranging from $Åk_2$ to $Åk_{25}$). The oxygen- and magnesium-isotopic compositions of the core and mantle are very different; typically, $\Delta^{17}O$ ~−26 ‰ and f_{Mg} (mass fractionation of Mg isotopes) ~10 ‰/amu in the core and $\Delta^{17}O$ ~−7 ‰ and f_{Mg} ~1 ‰/amu in most of the mantle. The chemical and O, Mg-isotopic data indicate that the core and mantle formed in separate events. Analyses of core and mantle phases plot along a single ^{26}Al–^{26}Mg isochron with initial $(^{26}Al/^{27}Al)_0$ corresponding to 4.8 ±1.0 (±2σ) × 10^{-5}, suggesting a similar formation age to normal CAIs in chondrites.

A conceivable scenario of the formation of Tama is as follows: (1) Melting of a precursor CAI at temperatures >1900 °C. The precursor would be a corundum-, hibonite-, spinel-bearing CAI. (2) Evaporation of Mg occurred from the liquid droplet, (3) Crystallization of nonstoichiometric Al-rich spinel and hibonite in the cooling liquid to form the core, (4) Condensation of melilite around the solidified core at a temperature of ~1200 °C. (5) Melting of the melilite by reheating to a temperature of ~1600 °C, and (6) mantle melilite crystallization from this liquid to fill cavities in the core.

Acknowledgements

We are grateful to John Wasson for his years of collaboration. His contribution to our lives and the cosmochemistry community is incalculable. Tama was found by him and this study was led by him. We thank H. Kojima for loaning us the thin section of Y-81020. We thank C. Park, S. Simon and A. N. Krot (Associate Editor) for constructive reviews and suggestions. We thank N. Kawasaki for numerous helpful discussions. We also thank G. J. MacPherson, H. Palme, G. R. Huss and A. M. Davis for constructive reviews of an early version of this manuscript. This work was supported by grants to HY by KagakuGijutsu-cho and Monbu-sho, to JTW by the US NSF and NASA (NNX10AG98G), and to AER by NASA (NNG06GF95G).

References

Aléon J. 2016. Oxygen isotopes in the early protoplanetary disk inferred from pyroxene in a classical type B CAI. *Earth and Planetary Science Letters* 440: 62–70.

Aléon J., El Goresy A., and Zinner E. 2007. Oxygen isotope heterogeneities in the earliest protosolar gas recorded in a meteoritic calcium-aluminum-rich inclusion. *Earth and Planetary Science Letters* 263: 114–127.

Aléon J., Krot A. N., McKeegan K. D., MacPherson G. J., and Ulyanov A. A. 2005. Fine-grained, spinel-rich inclusions from the reduced CV chondrite Efremovka: II. Oxygen isotopic compositions. *Meteoritics & PIunetary Science* 40: 1043–1058.

Armstrong J. T., Meeker G. P., Huneke J. C., and Wasserburg G. J. 1982. The Blue Angel: I. The mineralogy and petrology of a hibonite inclusion from the Murchison meteorite. *Geochimica et Cosmochimica Acta* 46: 575–595.

Beckett J. R. and Stolper E. 1994. The stability of hibonite, melilite, and other aluminous phases in silicate melts: Implications for the origin of hibonite-bearing inclusions from carbonaceous chondrites. *Meteoritics* 29: 41–65.

Bodénan J. D., Starkey N. A., Russell S. S., Wright I. P., and Franchi I. A. 2014. An oxygen isotope study of Wark- Lovering rims on type A CAIs in primitive carbonaceous chondrites. *Earth and Planetary Science Letters* 401: 327–336.

Catanzaro E. J., Murphy T. J., Garner E. L., and Shields W. R. 1966. Absolute isotopic abundance ratios and atomic weights of magnesium. *Journal of Research of the National Bureau of Standards* 70a: 453–458.

Clayton R. N. 1993. Oxygen isotopes in meteorites. *Annu. Rev. Earth Planet. Sci.* 21: 115–149.

Clayton R. N. and Mayeda T. K. 1999. Oxygen isotope studies of carbonaceous chondrites. *Geochimica et Cosmochimica Acta* 63: 2089–2104.

Clayton R. N., Onuma N., Grossman L., and Mayeda T. K. 1977. Distribution of the pre-solar component in Allende and other carbonaceous chondrites. *Earth and Planetary Science Letters* 34: 209–224.

Connelly J. N., Bizzarro M., Krot A. N., Nordlund Å., Wielandt D., and Ivanova M. A. 2012. The Absolute Chronology and Thermal Processing of Solids in the Solar Protoplanetary Disk. *Science* 338: 651-655.

Davis A. M., Hashimoto A., and Richter F. M. 1998. Isotopic mass fractionation under solar nebular conditions. *Meteoritics & Planetary Science* 33: A39.

De Aza A. H., Iglesias J. E., Pena P., and De Aza S. 2000. Ternary System Al_2O_3—MgO—CaO: Part II, Phase Relationships in the Subsystem Al_2O_3—$MgAl_2O_4$—$CaAl_4O_7$. *Journal of the American Ceramic Society* 83: 919-927.

El Goresy A., Palme H., Yabuki H., Nagel K., Herrwerth I., and Ramdohr P. 1984. A calcium-aluminum-rich inclusion from the Essebi (CM2) chondrite: Evidence for captured spinel-hibonite spherules and for an ultra-refractory rimming sequence. *Geochimica et Cosmochimica Acta* 48: 2283-2298.

Grossman L. and Larimer J. W. 1974. Early chemical history of the solar system. *Reviews of Geophysics* 12: 71-101.

Hallstedt B. 1992. Thermodynamic assessment of the system MgO-Al_2O_3. *Journal of the American Ceramic Society* 75: 1497-1507.

Han J., Brearley A. J., and Keller L. P. 2015. Microstructural evidence for a disequilibrium condensation origin for hibonite-spinel inclusions in the ALHA77307 CO3.0 chondrite. *Meteoritics & Planetary Science* 50: 2121-2136.

Hashimoto A. 1983. Evaporation metermorphism in the early solar nebula - evaporation experiments on the melt FeO-MgO-SiO_2-CaO-Al_2O_3 and chemical fractionations of primitive materials. *Geochemical Journal* 17: 111-145.

Ito M., Nagasawa H., and Yurimoto H. 2004. Oxygen isotopic SIMS analysis in Allende CAI: details of the very early thermal history of the solar system. *Geochimica et Cosmochimica Acta* 68: 2905-2923.

Itoh S., Kojima H., and Yurimoto H. 2004. Petrography and oxygen isotopic compositions in refractory inclusions from CO chondrites. *Geochimica et Cosmochimica Acta* 68: 183-194.

Katayama J., Itoh S., and Yurimoto H. 2012. Oxygen isotopic zoning of reversely zoned melilite crystals in a fluffy type A Ca-Al-rich inclusions from the Vigarano meteorite. *Meteoritics*

& Planetary Science 47: 2094–2106.

Kawasaki N., Itoh S., Sakamoto N., and Yurimoto H. 2017. Chronological study of oxygen isotope composition for the solar protoplanetary disk recorded in a fluffy Type A CAI from Vigarano. *Geochimica et Cosmochimica Acta* 201: 83-102.

Kawasaki N., Kato C., Itoh S., Wakaki S., Ito M., and Yurimoto H. 2015. ^{26}Al–^{26}Mg chronology and oxygen isotope distributions of multiple melting for a Type C CAI from Allende. *Geochimica et Cosmochimica Acta* 169: 99-114.

Kawasaki N., Sakamoto N., and Yurimoto H. 2012. Oxygen isotopic and chemical zoning of melilite crystals in a type A Ca-Al-rich inclusion of Efremovka CV3 chondrite. *Meteoritics & Planetary Science* 47: 2084–2093.

Kawasaki N., Simon S. B., Grossman L., Sakamoto N., and Yurimoto H. 2018. Crystal growth and disequilibrium distribution of oxygen isotopes in an igneous Ca-Al-rich inclusion from the Allende carbonaceous chondrite. *Geochimica et Cosmochimica Acta* 221: 318-341.

Kawasaki N., Wada S., Park C., Sakamoto N., and Yurimoto H. 2020. Variations in initial 26Al/27Al ratios among fine-grained Ca-Al-rich inclusions from reduced CV chondrites. *Geochimica et Cosmochimica Acta* 279: 1-15.

Kobayashi S., Imai H., and Yurimoto H. 2003. New extreme ^{16}O-rich reservoir in the early solar system. *Geochemical Journal* 37: 663-669.

Koike O., Yurimoto H., Nagasawa H., and Sueno S. 1993. Ion microprobe measurements of Mg isotopes in Type B1 CAI of Allende meteorite. *Proceedings of the NIPR Symposium on Antarctic Meteorites* 6: 357-363.

Krot A. N., Chaussidon M., Yurimoto H., Sakamoto N., Nagashima K., Hutcheon I. D., and MacPherson G. J. 2008. Oxygen isotopic compositions of Allende Type C CAIs: Evidence for isotopic exchange during nebular melting and asteroidal metamorphism. *Geochimica et Cosmochimica Acta* 72: 2534-2555.

Krot A. N., McKeegan K. D., Leshin L. A., MacPherson G. J., and Scott E. R. D. 2002. Existence of an ^{16}O-rich gaseous reservoir in the solar nebula. *Science* 295: 1051-1054.

Krot A. N., Nagashima K., Fintor K., and Pál-Molnár E. 2019. Evidence

for oxygen-isotope exchange in refractory inclusions from Kaba (CV3.1) carbonaceous chondrite during fluid-rock interaction on the CV parent asteroid. *Geochimica et Cosmochimica Acta*: 419–435.

Krot A. N., Nagashima K., Wasserburg G. J., Huss G. R., Papanastassiou D., Davis A. M., Hutcheon I. D., and Bizzarro M. 2014. Calcium-aluminum-rich inclusions with fractionation and unknown nuclear effects (FUN CAIs): I. Mineralogy, petrology, and oxygen isotopic compositions. *Geochimica et Cosmochimica Acta* 145: 206–247.

Larsen K. K., Trinquier A., Paton C., Schiller M., Wielandt D., Ivanova M. A., Connelly J. N., Nordlund Å., Krot A. N., and Bizzarro M. 2011. Evidence for magnesium Isotope Heterogeneity in the solar protoplanetary disk. *The Astrophysical Journal* 735: L37.

MacPherson G. J., Bar-Matthews M., Tanaka T., Olsen E., and Lawrence G. 1983. Refractory inclusions in the Murchison meteorite. *Geochimica et Cosmochimica Acta* 47: 823-839.

MacPherson G. J. and Davis A. M. 1994. Refractory inclusions in the prototypical CM chondrite, Mighei. *Geochimica et Cosmochimica Acta* 58: 5599-5625.

MacPherson G. J., Davis A. M., and Zinner E. K. 1995. The distribution of aluminum-26 in the early solar system: A reappraisal. *Meteoritics* 30: 365-386.

MacPherson G. J. and Grossman L. 1984. "Fluffy" Type A Ca-, Al-rich inclusions in the Allende meteorite. *Geochimica et Cosmochimica Acta* 48: 29-46.

MacPherson G. J., Grossman L., Hashimoto A., Bar-Matthews M., and Tanaka T. 1984. Petrographic studies of refractory inclusions from the Murchison meteorite. *Journal of Geophysical Research: Solid Earth* 89: C299-C312.

Makide K., Nagashima K., Krot A. N., Huss G. R., Hutcheon I. D., Hellebrand E., and Petaev M. I. 2013. Heterogeneous distribution of ^{26}Al at the birth of the Solar System: Evidence from corundum-bearing refractory inclusions in carbonaceous chondrites. *Geochimica et Cosmochimica Acta* 110: 190-215.

McKeegan K. D., Leshin L. A., Russell S. S., and MacPherson G. J. 1998. Oxygen isotope abundances in calcium-aluminum-rich

inclusions from ordinary chondrites; Implications for nebular heterogeneity. *Science* 280: 414-418.

Mendybaev R. A., Richter F. M., and Davis A. M. 2006. Crystallization of melilite from CMAS-liquids and the formation of the melilite mantle of Type B1 CAIs: Experimental simulations. *Geochimica et Cosmochimica Acta* 70: 2622–2642.

Park C., Wakaki S., Sakamoto N., Kobayashi S., and Yurimoto H. 2012. Oxygen isotopic composition of the solar nebula gas inferred from high-precision isotope imaging of melilite crystals in an Allende CAI. *Meteoritics & Planetary Science* 47: 2070–2083.

Sakai T. and Yurimoto H. 1999. Oxygen isotope distribution in CAIs of the Murchison meteorite. *Lunar and Planetary Science* 30: abs. 1528.

Sakamoto N., Seto Y., Itoh S., Kuramoto K., Fujino K., Nagashima K., Krot A. N., and Yurimoto H. 2007. Remnants of the early solar system water enriched in heavy oxygen isotopes. *Science* 317: 231-233.

Shirasuka K. and Yamaguchi G. 1974. Precise measurements of the crystal data and the solid-solution range of the defective spinel $MgO{\bullet}nAl_2O_3$. *Yogyo Kyokaishi* 82: 34-37.

Simon J. I., Hutcheon I. D., Simon S. B., Matzel J. E. P., Ramon E. C., Weber P. K., Grossman L., and DePaolo D. J. 2011. Oxygen isotope variations at the margin of a CAI records circulation within the solar nebula. *Science* 331: 1175-1178.

Simon J. I., Matzel J. E. P., Simon S. B., Hutcheon I. D., Ross D. K., Weber P. K., and Grossman L. 2016. Oxygen isotopic variations in the outer margins and Wark-Lovering rims of refractory inclusions. *Geochimica et Cosmochimica Acta* 186: 242–276.

Simon S. B., Grossman L., Hutcheon I. D., Phinney D. L., Weber P. K., and Fallon S. J. 2006. Formation of spinel-, hibonite-rich inclusions found in CM2 carbonaceous chondrites. *American Mineralogist* 91: 1675-1687.

Simon S. B., Yoneda S., Grossman L., and Davis A. M. 1994. A $CaAl_4O_7$-bearing refractory spherule from Murchison: Evidence for very high-temperature melting in the solar nebula. *Geochimica et Cosmochimica Acta* 58: 1937-1949.

Ushikubo T., Kimura M., Kita N. T., and Valley J. W. 2012. Primordial

oxygen isotope reservoirs of the solar nebula recorded in chondrules in Acfer 094 carbonaceous chondrite. *Geochimica et Cosmochimica Acta* 90: 242-264.

Ushikubo T., Tenner T. J., Hiyagon H., and Kita N. T. 2017. A long duration of the ^{16}O-rich reservoir in the solar nebula, as recorded in fine-grained refractory inclusions from the least metamorphosed carbonaceous chondrites. *Geochimica et Cosmochimica Acta* 201: 103–122.

Viechnicki D., Schmid F., and McCauley J. W. 1974. Liquidus-Solidus Determinations in the System $MgAl_2O_4$-Al_2O_3. *Journal of the American Ceramic Society* 57: 47-48.

Viertel H. U. and Seifert F. 1980. Thermal stability of difect spinels in the system $MgAl_2O_4$-Al_2O_3. *Neues Jahrbuch für Mineralogie* 140: 89-101.

Wada S., Kawasaki N., Park C., and Yurimoto H. 2020. Melilite condensed from an ^{16}O-poor gaseous reservoir: Evidence from a fine-grained Ca-Al-rich inclusion of Northwest Africa 8613. *Geochimica et Cosmochimica Acta* 288: 161-175.

Wakaki S., Itoh S., Tanaka T., and Yurimoto H. 2013. Petrology, trace element abundances and oxygen isotopic compositions of a compound CAI-chondrule object from Allende. *Geochimica et Cosmochimica Acta* 102: 261-279.

Wasson J. T., Yurimoto H., and Russell S. S. 2001. ^{16}O-rich melilite in CO3.0 chondrites: possible formation of common, ^{16}O-poor melilite by aqueous alteration. *Geochimica et Cosmochimica Acta* 65: 4539-4549.

Yoneda S. and Grossman L. 1995. Condensation of CaO-MgO-Al_2O_3-SiO_2 liquids from cosmic gases. *Geochimica et Cosmochimica Acta* 59: 3413-3444.

Yoshitake M., Koide Y., and Yurimoto H. 2005. Correlations between oxygen-isotopic composition and petrologic setting in a coarse-grained Ca, Al-rich inclusion. *Geochimica et Cosmochimica Acta* 69: 2663-2674.

Yurimoto H., Ito M., and Nagasawa H. 1998. Oxygen isotope exchange between refractory inclusion in Allende and solar nebula gas. *Science* 282: 1874-1877.

Yurimoto H., Krot A. N., Choi B.-G., Aleon J., Kunihiro T., and Brearley A. J. 2008. Oxygen Isotopes of Chondritic Components.

Reviews in Mineralogy and Geochemistry 68: 141-186.

Yurimoto H., Nagasawa H., Mori Y., and Matsubaya O. 1994. Micro-distribution of oxygen isotopes in a refractory inclusion from the Allende meteorite. *Earth and Planetary Science Letters* 128: 47-53.

Table 1. Representative mineral compositions (wt%) and the cation numbers in Tama and a nearby spinel-melilite-CAI.

mineral	site	SiO2	TiO2	Al2O3	FeO	MgO	CaO	Total	O	Si	Ti	Al	Fe	Mg	Ca	Total
Tama																
hibonite	core	0.19	3.10	86.20	0.38	2.70	7.50	100.07	19	0.021	0.261	11.368	0.036	0.450	0.899	13.034
	core	0.11	8.40	77.70	0.14	3.50	8.10	97.95	19	0.013	0.731	10.595	0.014	0.603	1.004	12.959
	core	<0.04	4.20	83.70	0.41	2.00	8.20	98.51	19	0.000	0.361	11.264	0.039	0.340	1.003	13.007
melilite	core	22.20	0.14	36.00	0.15	0.14	39.80	98.43	7	1.028	0.005	1.964	0.006	0.010	1.973	4.985
	B	22.80	<0.04	34.20	0.43	0.75	40.10	98.28	7	1.061	0.000	1.875	0.017	0.052	1.998	5.002
	D	25.60	0.08	28.60	0.36	2.70	39.80	97.14	7	1.204	0.003	1.585	0.014	0.189	2.005	5.000
	D/E	24.00	0.08	32.20	0.68	1.50	39.40	97.86	7	1.120	0.003	1.770	0.027	0.104	1.969	4.992
Spinel(ss)	core	<0.04	0.85	75.50	1.40	20.50	0.06	98.31	4	0.000	0.015	2.137	0.028	0.734	0.002	2.916
	core	<0.04	0.68	90.40	0.33	7.70	0.09	99.20	4	0.000	0.012	2.468	0.006	0.266	0.002	2.754
Al-patch	core	<0.04	0.76	94.90	0.32	2.90	0.30	99.18	3	0.000	0.010	1.930	0.005	0.075	0.006	2.025
	core	<0.05	0.46	99.50	0.44	0.25	0.09	100.79	3	0.000	0.006	1.982	0.006	0.006	0.002	2.002
perovskite	core	0.68	55.10	1.20	2.40	0.07	38.30	97.75	3	0.016	0.960	0.033	0.047	0.002	0.951	2.008
grossite	sat	0.40	0.61	77.60	1.10	1.30	15.50	96.51	7	0.018	0.020	4.043	0.041	0.086	0.734	4.941
Adjacent spinel-melilite CAI																
spinel	CAI	<0.04	0.22	70.60	0.26	27.30	0.24	98.62	4	0.000	0.004	2.001	0.005	0.978	0.006	2.995
	CAI	<0.04	3.00	66.90	0.39	26.50	2.20	98.99	4	0.000	0.055	1.912	0.008	0.957	0.057	2.989

site: location in Fig. 1, sat: core satellite fragment on left side of mantle, spinel(ss): non-stoichiometric spinel, Al-patch: alumina-rich patch, CAI: spinel-melilite-CAI of upper right of Tama (see Fig. 1). All analyses were measured by wave-length-dispersive type electron-probe micro-analyzer. Concentrations of other elements were less than 0.1wt% from X-ray spectra by energy-dispersive type electron-probe micro-analyzer.

Table 2. Results of O-isotope analyses (‰).

anal#	$\delta^{17}O_{SMOW}$	$2\sigma_m$	$\delta^{18}O_{SMOW}$	$2\sigma_m$	$\Delta^{17}O$	$2\sigma_m$	Remarks
hibonite							
#10	-57.9	4.9	-53.8	2.8	-29.9	5.6	
#03	-50.0	4.1	-50.5	2.1	-23.8	4.6	
#03-2	-55.7	4.5	-56.1	1.9	-26.5	4.9	
#03-3	-51.6	5.4	-48.5	2.4	-26.4	5.9	
spinel							
#08	-53.0	4.9	-53.0	2.6	-25.4	5.5	
#08-2	-53.6	4.6	-53.0	2.5	-26.0	5.2	
mantle melilite							
grain A							Åk%
#01	-9.5	4.9	-1.7	2.6	-8.6	5.6	11
#05	-4.8	4.6	0.4	1.9	-5.0	5.0	13
#07	-11.9	5.4	-4.1	2.7	-9.8	6.1	13
#14-3	-3.4	5.9	2.3	3.5	-4.6	6.9	8
#15	2.5	5.2	8.3	3.3	-1.8	6.1	9
#17	-27.0	4.6	-23.2	3.3	-15.0	5.7	3
#20	-10.5	4.5	-8.2	2.0	-6.2	4.9	14
#20-2	-9.7	4.6	-5.0	2.6	-7.1	5.3	14
grain B							
#12	-25.0	4.4	-21.2	2.4	-13.9	5.0	3
#13	-25.3	4.5	-22.5	2.1	-13.6	5.0	2
grain C							
#16	-27.3	4.3	-20.4	3.2	-16.7	5.3	4
grain D							
#22	3.8	5.5	15.5	3.2	-4.3	6.4	13
#23	-12.0	4.7	-5.8	3.3	-8.9	5.8	7
grain E							
#24	-36.1	4.9	-33.8	2.7	-18.6	5.6	3
grain F							
#21	-20.8	4.8	-18.1	2.1	-11.3	5.2	4
grain G							
#25	-42.3	4.9	-41.3	2.4	-20.8	5.5	2
core melilite							
#04	-34.2	5.3	-34.7	2.0	-16.1	5.7	2
#06	-6.9	4.9	0.2	2.3	-7.0	5.5	2
#09	-46.4	4.6	-39.5	2.7	-25.8	5.3	1
mixed phases							composition
#02	-52.7	3.7	-53.7	2.2	-24.8	4.3	sp50hib50
#11	-29.9	4.8	-26.5	2.3	-16.2	5.3	mel60sp40
#18	-29.7	4.4	-27.6	2.3	-15.4	4.9	hib70acc30
#19	-1.6	4.7	3.5	2.7	-3.4	5.4	mel50acc50
#26	4.0	6.1	11.1	2.5	-1.7	6.6	acc80mel20

$\Delta^{17}O = \delta^{17}O_{SMOW} - 0.52\ \delta^{18}O_{SMOW}$. σ_m: standard deviation of the mean based on statistics of secondary ion intensity. Åk%: åkermanite content. sp: spinel, hib: hibonite, mel: melilite, acc: accretionary rim.

Table 3. Results of Mg-isotope analyses.

anal#	$^{27}Al/^{24}Mg$	2σ	f_{Mg} (‰/amu)	$2\sigma_m$	$\delta^{26}Mg$* (‰)	$2\sigma_m$
hibonite						
#03	15.9	0.6	11.3	2.1	6.0	2.8
#10	17.0	0.4	31.4	2.2	5.7	3.4
spinel						
#08*	3.3	0.1	12.2	0.5	4.0	1.5
mantle melilite						
grain A						
#01	36.5	0.8	1.1	3.9	10.7	7.4
#05*	21.3	0.6	2.2	0.8	5.8	2.8
#07	16.4	1.4	2.7	3.3	7.6	6.1
#17	63.2	4.8	-4.1	4.7	32.3	10.5
#20**	18.7	1.2	3.3	5.0	6.2	2.3
grain D						
#22	14.7	1.4	0.9	2.8	7.3	5.2
#23**	32.9	1.4	-1.0	1.6	14.9	3.7
grain E						
#24**	45.9	11.5	3.4	3.9	16.1	7.9
grain F						
#21	74.3	2.1	5.1	4.8	20.0	9.9
grain G						
#25**	87.6	13.3	1.2	6.4	33.7	7.3
core melilite						
#09	166	10	-2.1	7.7	73	18

f_{Mg}: intrinsic mass fractionation from terrestrial value. $\delta^{26}Mg$*: Excess ^{26}Mg from terrestrial value. σ: standard deviation. σ_m: standard deviation of the mean based on statistics of secondary ion intensity. *average of two analyses. **average of three analyses.

Figure captions

Fig. 1. (a) Backscatter electron image of Tama from the Y81020 CO3 chondrite. Numbers in the image correspond to SIMS analysis points listed in Tables 2 and 3. (b) Transmitted light micrograph of Tama (crossed polars with sensitive color plate). Sputtering craters by SIMS are observed as bright spots. (c) Composition image of Tama and a spinel-melilite CAI. Nonstoichiometric spinel grains having Al-excess are distributed in the core of Tama. Lines in mantle melilite in Tama indicate grain boundaries between the crystals; letters A to G are assigned to these grains. Several small patches on the left edge of the mantle contain hibonite, Al-rich spinel, and the alumina-rich patch (core satellites). Above and to the left of Tama (separated from it by a dark region in Fig. 1c), is a spinel-melilite CAI in which the spinel is nearly stoichiometric (Table 1). The O-isotopic compositions of all minerals (spinel, melilite and Al, Ti-rich diopside) in the spinel-melilite CAI are ^{16}O-rich ($\Delta^{17}O \approx -26‰$). The characteristics of the spinel-melilite CAI are the same as those typical of refractory inclusions in Y81020 (Itoh et al., 2004).

Fig. 2. Spinel solid solution showing an excess of Al-site cations and a deficit of Mg-site cations relative to stoichiometric $MgAl_2O_4$. Plots of Al_2O_3-rich patch in Tama correspond to the bulk compositions of mixture phases.

Fig. 3. Oxygen isotopic compositions of Tama. Errors are $2\sigma_m$. Core hibonite and spinel form a cluster with $\delta^{17}O$ and $\delta^{18}O$ values $\leq -48‰$. Melilites form an array extending from this cluster to near the intersection of the CCAM and TF lines. CCAM:

carbonaceous chondrite anhydrous minerals (Clayton and Mayeda, 1999; Clayton et al., 1977), TF: terrestrial fractionation (Clayton, 1993), PCM: primitive chondrule minerals (Ushikubo et al., 2012), Slope-1: connecting line between cosmic symplectites and the most ^{16}O-rich chondrule (Kobayashi et al., 2003; Sakamoto et al., 2007).

Fig. 4. Oxygen-isotopic composition vs. melilite composition of Tama. Errors are $2\sigma_m$ ○: mantle melilite grain #A, ●: other grains of mantle melilite, □: core melilite. Melilite with Åk content >6 mol% has constant Δ^{17}O and Åk<5 correlates with Δ^{17}O.

Fig. 5. Al-Mg systematics in Tama. Errors are 2σ for x-axis and $2\sigma_m$ for y-axis, respectively. The error on the initial Al ratio is also $2\sigma_m$.

Fig. 6. Projection of the liquidus surface of the system Al_2O_3-MgO-CaO (De Aza et al., 2000). Al_2O_3: corundum, $MgAl_2O_4$: spinel, $MgAl_2O_4$(ss): spinel solid solution, CA_6: hibonite, CA_2: grossite, open circle: core composition of Tama, solid circle: core composition of Tama without melilite. B6: bulk composition of CAI B6 (Simon et al., 1994), BB-2: bulk composition of CAI BB-2 (MacPherson et al., 1983). Compositions are in wt% oxide; temperatures are in ˚C inferred from De Aza et al. (2000). B6: A CAI of spinel-hibonite spherule from Murchison CM2. The CAI consists of grossite, perovskite, spinel and hibonite rimmed by a melilite-anorthite-diopside layer. The excess ^{26}Mg was observed from grossite. The initial $(^{26}Al/^{27}Al)_0$ ratio is 2.91 ±0.78 (2σ) $\times10^{-5}$. (Simon et al., 1994). BB-2: A CAI of spinel-hibonite spherule from Murchison CM2. The CAI consists of spinel, hibonite and perovskite

(MacPherson et al., 1983).

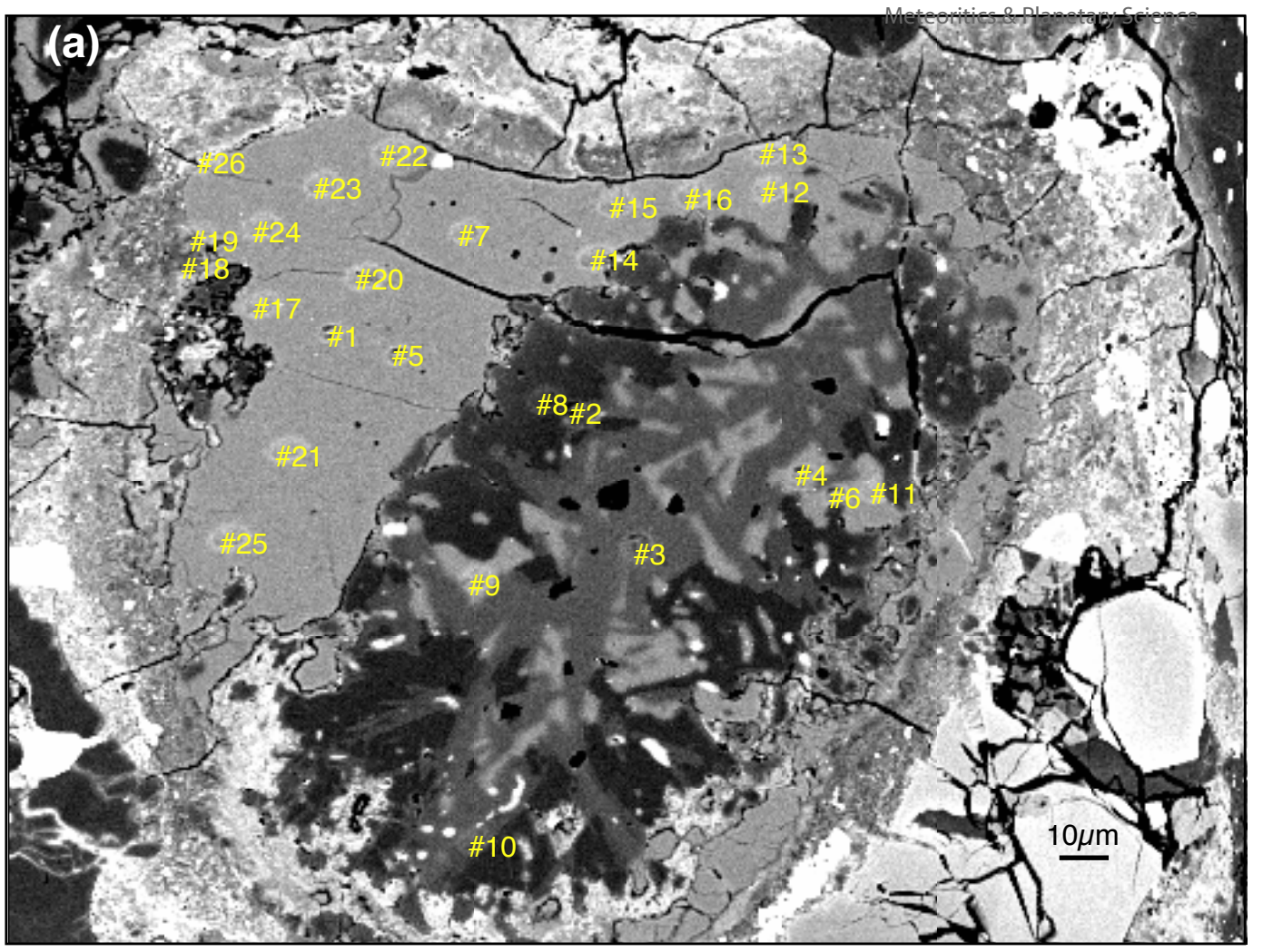

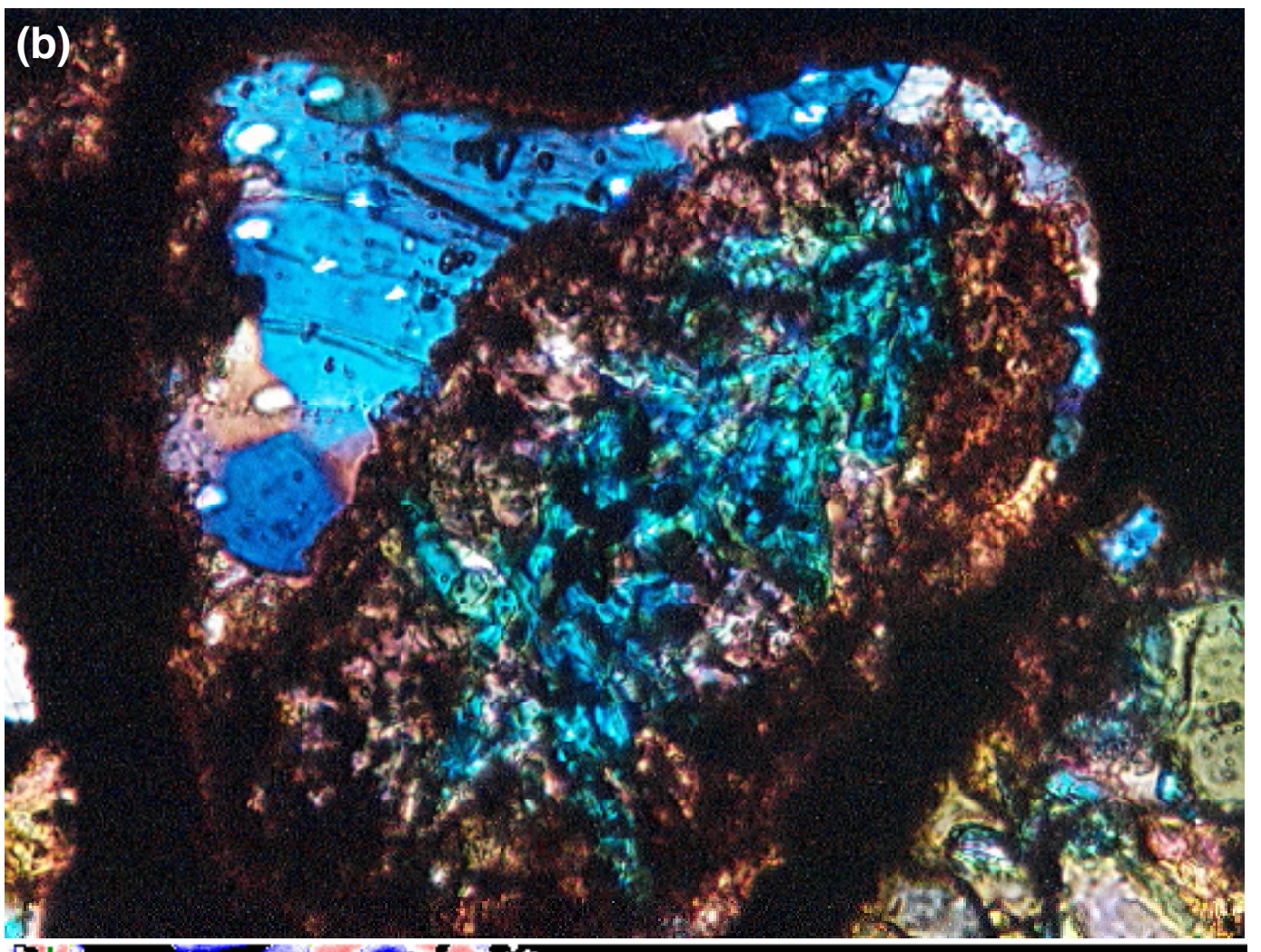

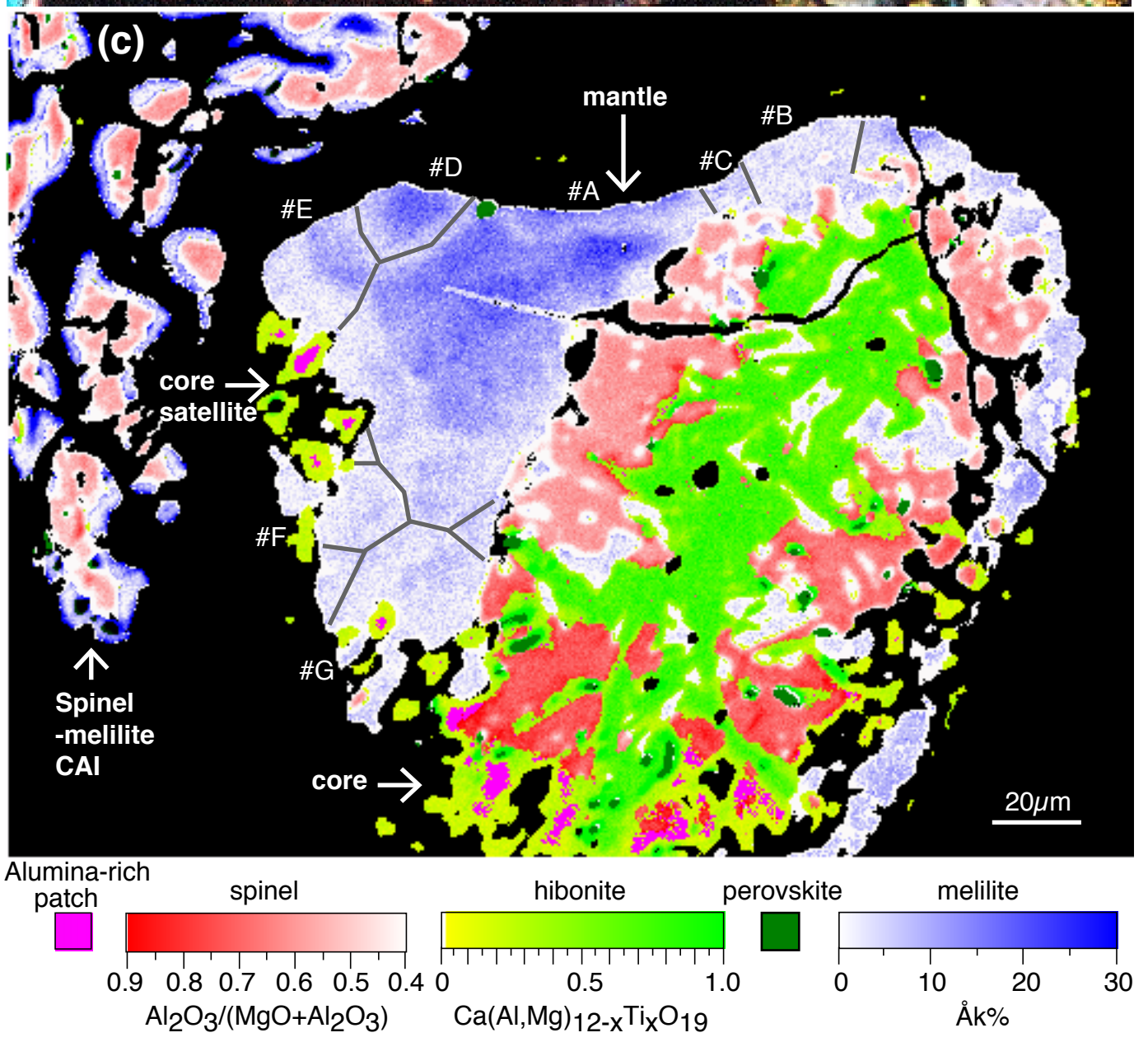

Yurimoto et al. Fig. 1

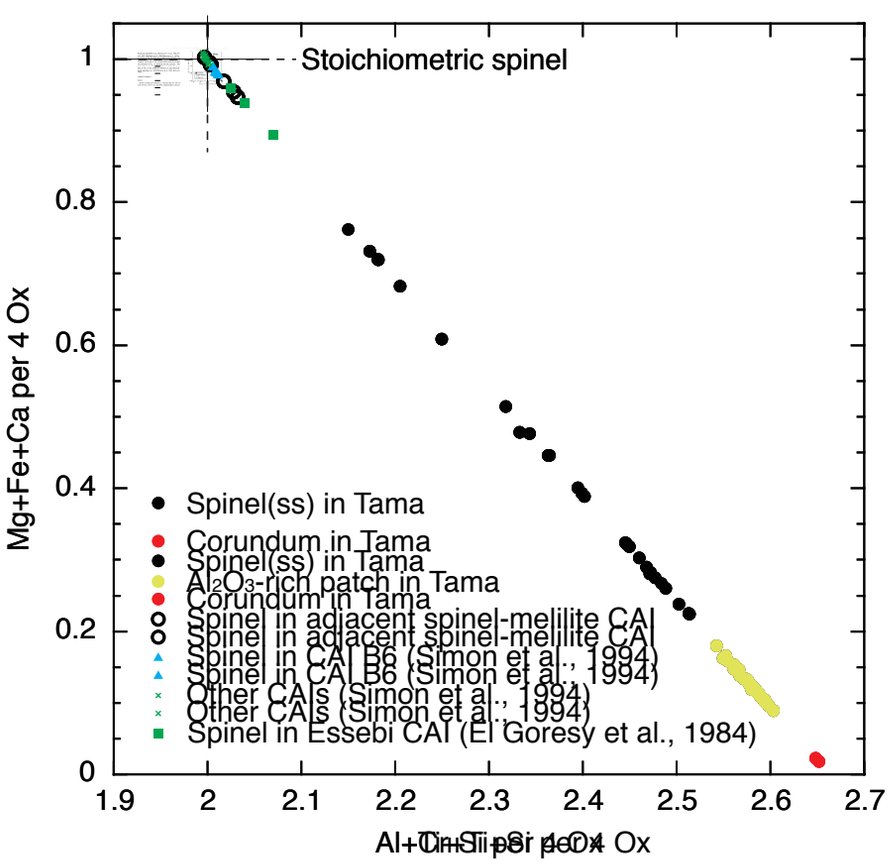
Stoichiometric spinel
Mg+Fe+Ca per 4 Ox
Al+Cr+Ti per 4 Ox
1
0.8
0.6
0.4
0.2
0
1.9
2
2.1
2.2
2.3
2.4
2.5
2.6
2.7
Spinel(ss) in Tama
Corundum in Tama
Spinel(ss) in Tama
Al2O3-rich patch in Tama
Corundum in Tama
Spinel in adjacent spinel-melilite CAI
Spinel in adjacent spinel-melilite CAI
Spinel in CAI B6 (Simon et al., 1994)
Spinel in CAI B6 (Simon et al., 1994)
Other CAIs (Simon et al., 1994)
Other CAIs (Simon et al., 1994)
Spinel in Essebi CAI (El Goresy et al., 1984)

Fig. 2

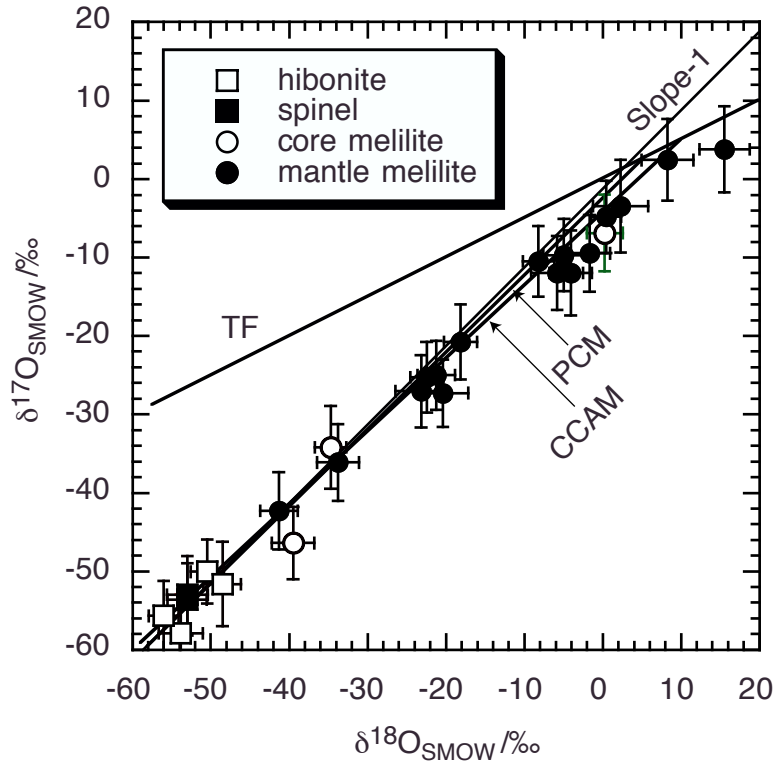

Yurimoto et al. Fig. 3

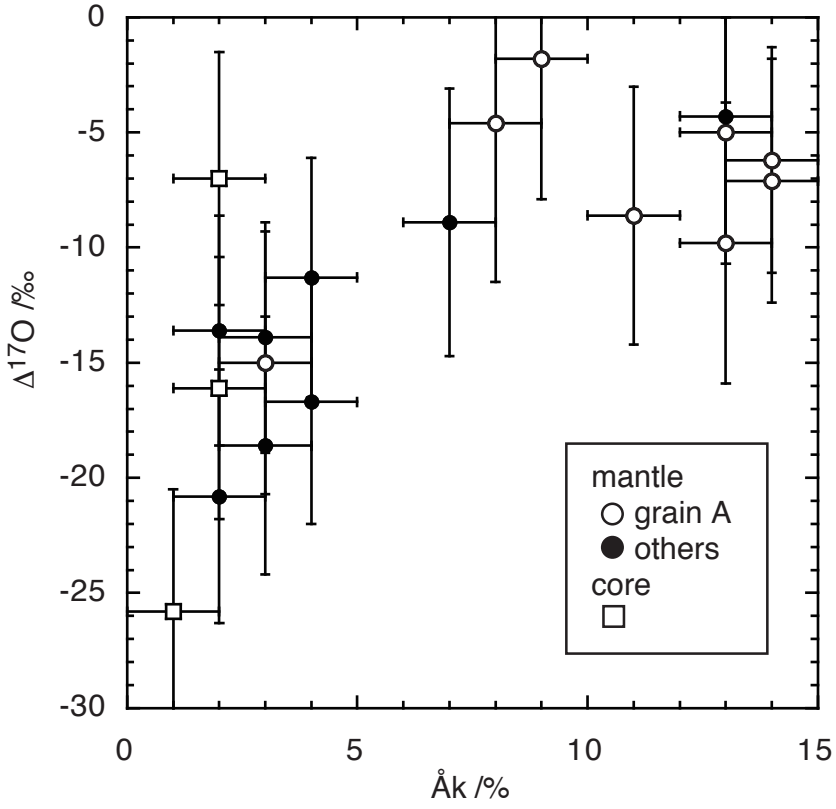

Yurimoto et al. Fig. 4

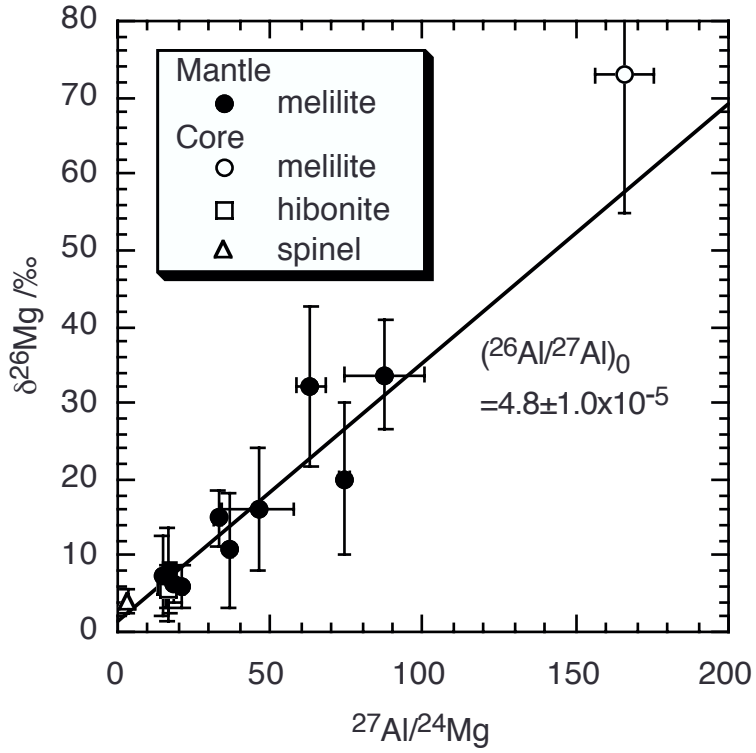
Mantle
melilite
Core
melilite
hibonite
spinel
$(^{26}Al/^{27}Al)_0$
$=4.8\pm1.0\times10^{-5}$
$\delta^{26}Mg$ /‰
$^{27}Al/^{24}Mg$
0
10
20
30
40
50
60
70
80
0
50
100
150
200

Fig. 5

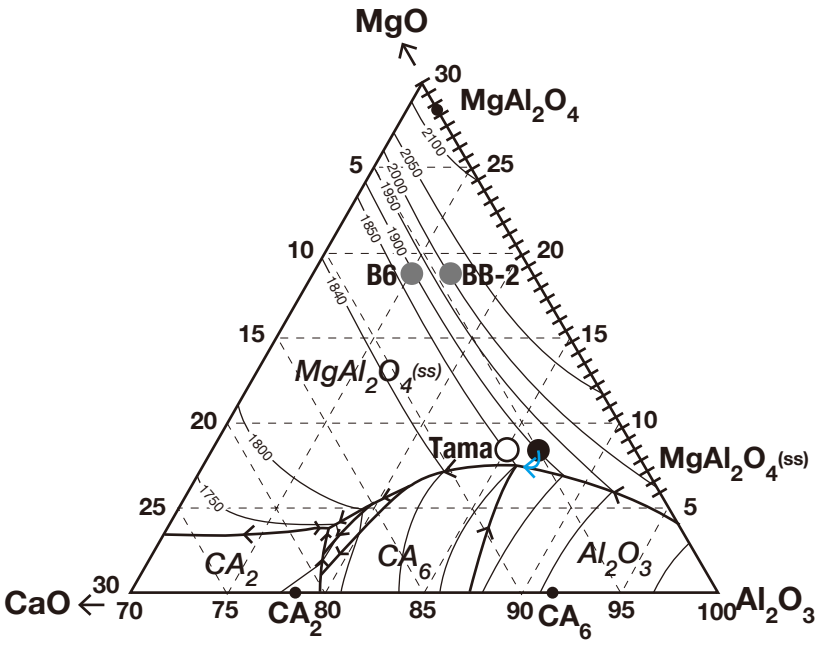
MgO
MgAl2O4
CaO
Al2O3
CA2
CA6
MgAl2O4(ss)
Tama
B6
BB-2
CA2
CA6
Al2O3
MgAl2O4(ss)
30
25
20
15
10
5
70
75
80
85
90
95
100
2100
2050
2000
1950
1900
1850
1840
1800
1750

Fig. 6